Soft robotic surfaces and bodies with reconfigurable topologies based on a monolithically printed pneumatic cell

Alan N. Pham[1], Pratap Rao[1], Cagdas D. Onal[2]

[1]Department of Mechanical Engineering, Worcester Polytechnic Institute, Worcester, MA 01609, USA

[2]Department of Robotics Engineering, Worcester Polytechnic Institute, Worcester, MA 01609, USA

Soft robots can achieve compliant motion, but most are fabricated as bodies with fixed size, topology, and function. A route to adaptable soft robots is to build them from actuated units that can be reconfigured into multiple topologies while preserving continuous deformation. Here we show a soft robotic architecture with reconfigurable topologies based on a monolithically printed, pneumatically actuated cellular unit that integrates actuation, compliant linkage motion, and modular connectivity. In planar arrays, pressure-driven cell expansion and module-scale bending bias produce controlled three-dimensional surface morphing, including multi-feature shape display, overhang generation, and object interaction. Reconfiguring the same building block into cylindrical topologies yields continuum-style bending and grasping, peristaltic locomotion, and self-rolling locomotion. The results show how changing topology and actuation pattern, rather than redesigning the cellular unit for each task, allows one manufacturable architecture to generate multiple soft robotic morphologies and functions.

1 Introduction

Soft robots are often fabricated as task-specific bodies with fixed size, connectivity, and morphology. When the required task or body plan changes, adaptation usually requires redesign and refabrication. A more scalable route is a soft robotic architecture built from repeated units that can be manufactured once and reconfigured into different topologies; in this route, the same local actuator is reused while module connectivity and actuation pattern set the response of the surface or body (*1–3*).

This goal remains difficult because the architecture must combine continuous shape change, distributed actuation, scalable fabrication, and topology-level reconfiguration (*1*, *4*). Important progress has been made on each part of this problem. Voxel-based soft robots and modular soft building blocks show how compliant robots can be configured from repeated components (*5–7*). Compact soft surfaces and shape displays show how dense arrays can render height fields, tune stiffness, and interact with objects (*8–16*). Soft continuum robots can bend, grasp, and locomote (*17–23*). The remaining gap is a single soft robotic building block that is locally actuated, manufactured as a monolithic pneumatic unit, assembled as a continuous morphing surface, and then reconfigured into planar and non-planar robot bodies without redesigning the actuator.

One route to this system is to encode shape-generating behavior in the geometry of a cell that is arrayed in a tessellated fashion. Mechanical metamaterials and buckling-based bistable systems have shown that geometry can program deformation, stiffening, and deployed states, but in many of these systems the geometry defines a fixed response once fabricated. They therefore do not provide the local pneumatic controllability needed to tune multiple robotic behaviors from the same unit (*24–27*). In contrast, we sought a cellular unit that is manufacturable, pneumatically actuated, compatible with tessellated arrays, and able to convert local expansion into a range of controlled out-of-plane morphologies. The Sarrus linkage provides a useful basis because lateral expansion is accompanied by leg rotation and geometry-dependent mechanical response (*28*). Sarrus-based systems have also been explored in reconfigurable metamaterial arrays (*28*, *29*), self-folding modular machines (*30*), and millimeter-scale articulated devices (*31*, *32*).

Here we introduce a soft robotic architecture with reconfigurable topologies based on a monolithically 3D-printed, pneumatically actuated cellular unit with integrated actuation and modular connectivity. The key advance is the use of a repeated pneumatic cell as both a controlled surface-morphing primitive and a reconfigurable robot-body primitive, linking capabilities that are usually developed in separate

systems. Repeated use of this unit converts in-plane cell expansion into controlled three-dimensional shape change through module-scale bending bias. Planar assemblies generate continuous surface morphing, multi-feature shape display, overhang formation, and object interaction. Cylindrical assemblies generate continuum-style bending, grasping, peristaltic locomotion, and self-rolling locomotion. The same manufacturable cellular architecture therefore supports multiple larger-scale robotic functions by changing topology and actuation pattern, rather than redesigning the cellular actuator and connection scheme for each task.

2 Results

The Results are organized around three explicit levels of the architecture: the cell/module level, where pressure-driven expansion and bending bias are established; the planar-array level, where actuation patterns generate controlled surface features and object interactions; and the cylindrical-robot level, where the same modules are reconfigured into bending, grasping, peristaltic, and rolling bodies.

2.1 Mechanical characterization

Cell-level characterization

We first characterize the cell that serves as the building block of the system. Figure 1 compares uncapped and capped cell variants across the actuation range, quantifies the pressure-dependent expansion ratio, and shows the cross-sectional and isometric cell geometry. These measurements establish the basic conversion from pneumatic pressure to repeatable in-plane expansion, while the geometry views separate the internal compliant Sarrus linkage and integrated PneuNet actuator from the capped external cell geometry. The isolated cell primarily serves as a unit for pressure-driven in-plane expansion; by itself, however, it does not provide the controlled out-of-plane bending bias required for array-level shape formation.

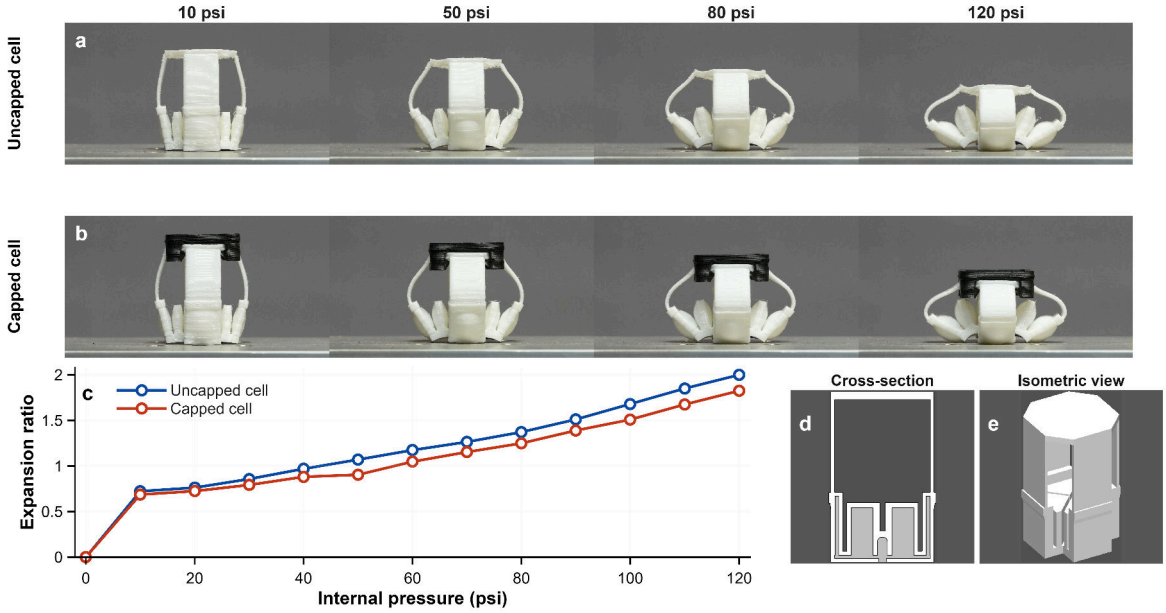

Figure 1. Cell geometry and pressure-driven expansion. (a,b) Uncapped and capped cells across the actuation range. (c) Pressure-dependent lateral expansion ratio for both cell variants, showing that the capped cell preserves the same expansion mechanism while reducing open gaps at the top surface. (d) Cross-section of the uncapped cell core showing the compliant Sarrus linkage and integrated PneuNet actuator; the cap is not included in this cross-section. (e) Isometric view of the capped cell geometry showing cap placement.

Module-level characterization

We therefore next examine how cells behave when assembled into modules. Each module consists of a 2×2 arrangement of four interconnected cells. At the module level, the architecture introduces the directional bias needed for reproducible out-of-plane buckling. Figure 2 shows single-module and two-module configurations across the actuation range. In addition to the expansion of each cell, the assembled module bends during actuation; Figure 2c tracks this response using the single-module bending angle θ_s and the two-module bending angle θ_d, indicated in Figure 2a,b. Each angle is measured as the local side-view tilt of the actuated module relative to a horizontal reference. This pressure-dependent module bending provides the geometric bias that favors buckling in a consistent direction. In the 80 psi views of Figure 2a,b, the upright-V and inverted-V linkage leg pairs formed during actuation are marked directly on the modules. Figure 2d shows the unactuated module cross-section with the cross-cell pneumatic channels, and Figure 2e shows the corresponding isometric module view. This result is the mechanical bridge between the cell-scale expansion in Figure 1 and the larger shape displays developed in the following sections.

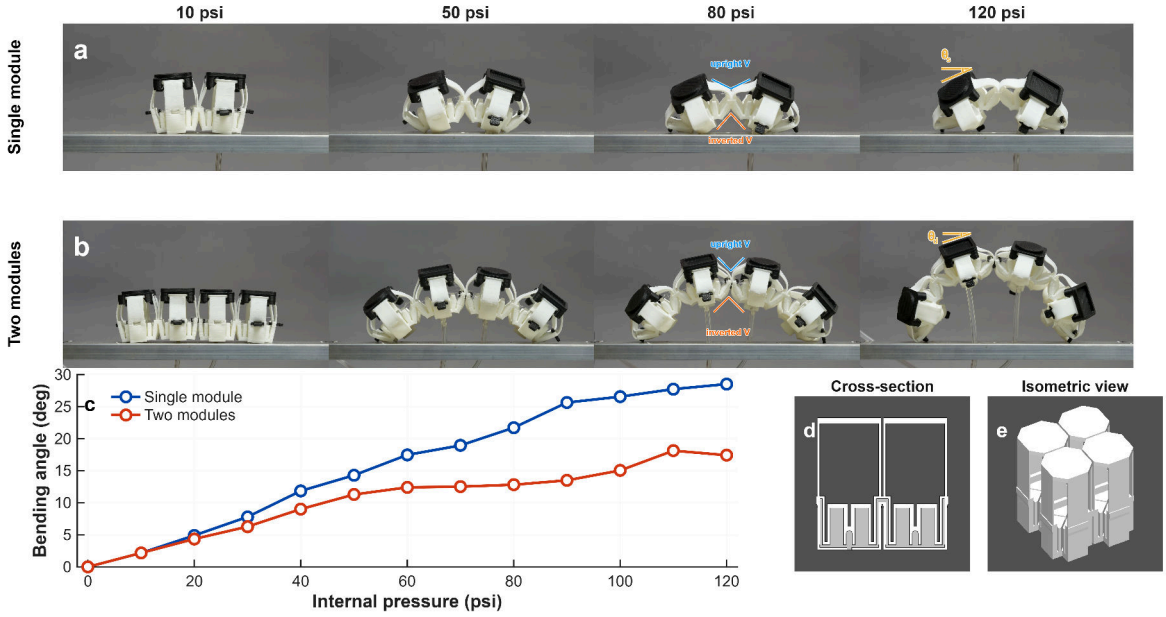

Figure 2. Directional bending in the 2×2 module. (a) Single-module side views across the actuation range; the angle marker defines the single-module bending angle, θ_s, as the local tilt of the actuated module relative to a horizontal reference. The 80 psi view marks the upright-V and inverted-V linkage leg pairs that form during actuation. (b) Two joined modules actuated over the same pressure range; the angle marker defines the corresponding two-module bending angle, θ_d, while showing that the same V-shaped leg-pair geometry persists across module connections. (c) Measured θ_s and θ_d as functions of internal pressure. (d) Unactuated module cross-section showing the cross-cell pneumatic channels and linkage-leg geometry. (e) Isometric view of the 2×2 module geometry.

We then characterized the force response of both the individual cell and the assembled array. Figure 3 shows representative uncompressed, half-compressed, and fully compressed states for the uncapped cell, capped cell, and 3×3 module array, defining the deformation states used for the quantitative force measurements. The lateral ends of the cell were compressed at a constant displacement rate while measuring the resisting force across the full range of actuation pressures. A similar test was performed on a small 3×3 module array, compressing from the actuated height to the unactuated height. All array-level mechanical tests were performed under constrained boundary conditions to suppress free lateral motion and enforce out-of-plane deformation.

After full compression was achieved, the cells or array were unloaded until they returned to their original state, forming the hysteresis loops shown in Figure 4. Here, hysteresis refers to the difference between the loading and unloading force responses at the same displacement. The array-level loops are more pronounced, particularly in panel c of Figure 4, where the loading path produces higher measured force than the unloading path. In practical terms, the measured force of the assembled array depends more strongly on whether the array is being compressed or released than it does for a single cell, so quasi-static force measurements should be compared with sequential-actuation demonstrations using the loading history in mind.

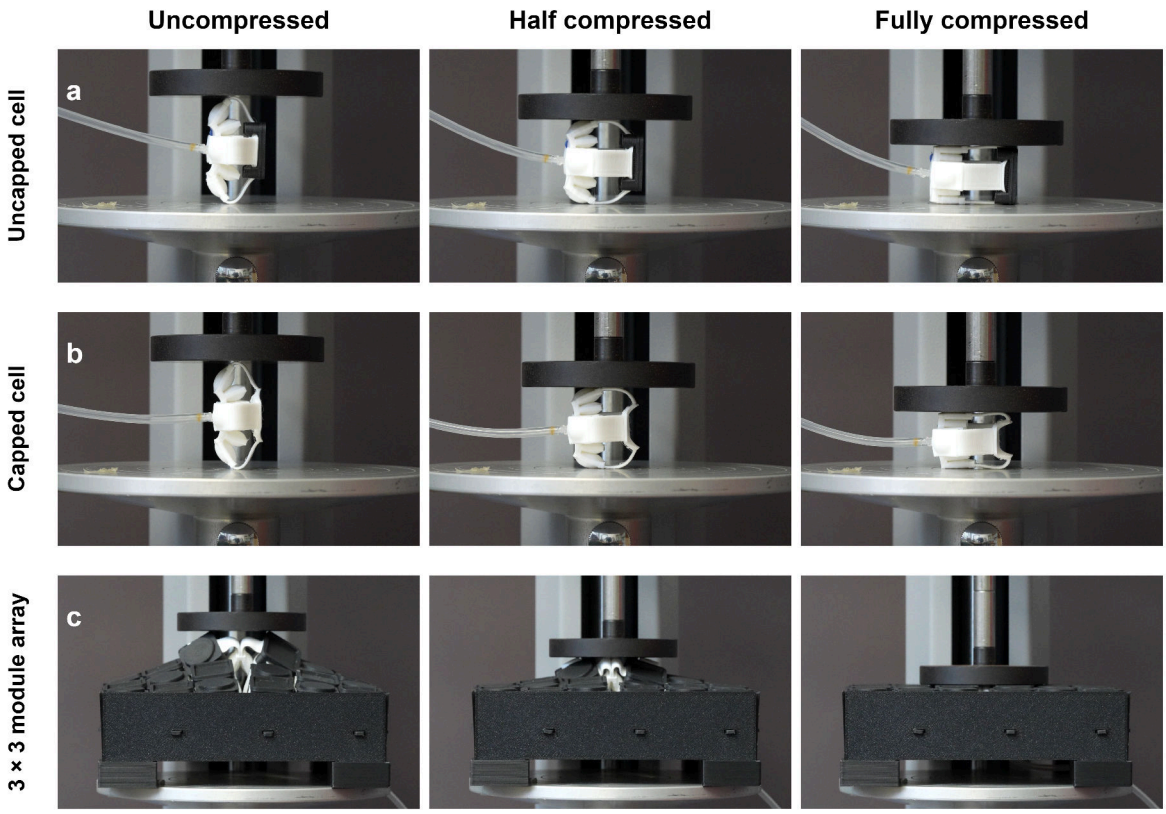

Figure 3. Representative compression states used for mechanical testing. (a) Uncapped cell, (b) capped cell, and (c) 3 × 3 module array shown in unloaded, half-compressed, and fully compressed states. These images define the compression stroke used for the force-displacement and hysteresis measurements.

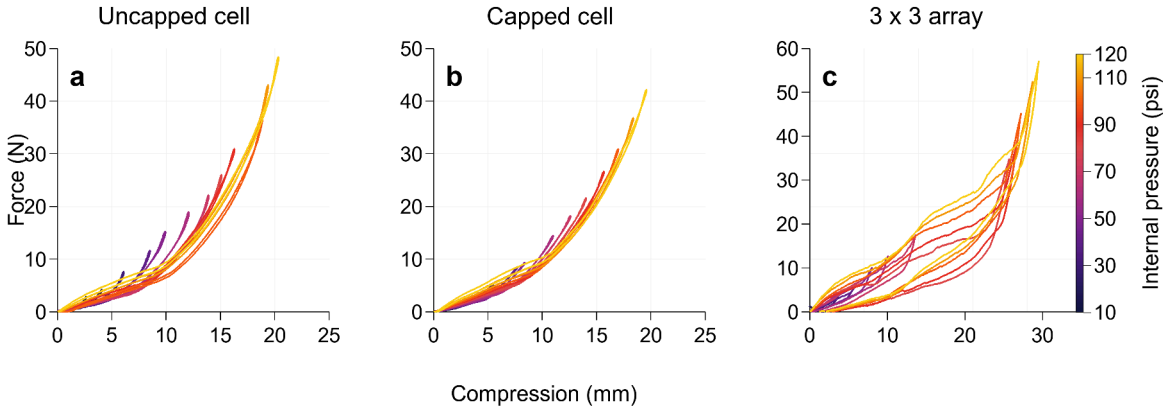

Figure 4. Pressure-dependent force-displacement hysteresis. (a,b) Uncapped and capped cells were compressed from their fully actuated width to the unactuated width and then unloaded to the initial width. (c) A 3 × 3 module array was compressed from maximum dome height to the unactuated height and then unloaded. Hysteresis is defined as the difference between loading and unloading force at the same displacement; the array shows the largest separation between the two paths.

Stiffness was determined from the local slope of the force-displacement response. Figure 5 shows pressure-dependent variable stiffness at both the cell and array levels, linking actuation pressure to

load-bearing behavior rather than only to shape. In the capped and uncapped cells, stiffness is lowest at intermediate widths and increases as the cell becomes either wider or narrower. This minimum occurs at 37 mm for the uncapped cell and 35 mm for the capped cell. The trend is consistent with geometry-dependent changes in how the Sarrus linkage legs resist compression during actuation. At higher pressures, the legs become more aligned with the compression direction, shifting the mechanical response toward axial loading; at lower actuation states, the legs are oriented more perpendicularly, and the response is more strongly governed by bending. The capped cell shows a less smooth stiffness profile in Figure 5e, consistent with additional interactions between the cap and the underlying linkage.

For the array, the peak stiffness also occurs near maximum compression. Unlike the single-cell case, however, the 3×3 module array exhibits multiple regions of increasing and decreasing stiffness over the compression stroke. This response reflects the combined contribution of many cells with different local linkage orientations: as compression proceeds, some regions remain bending-dominated while others become more aligned with the loading direction and shift toward axial resistance.

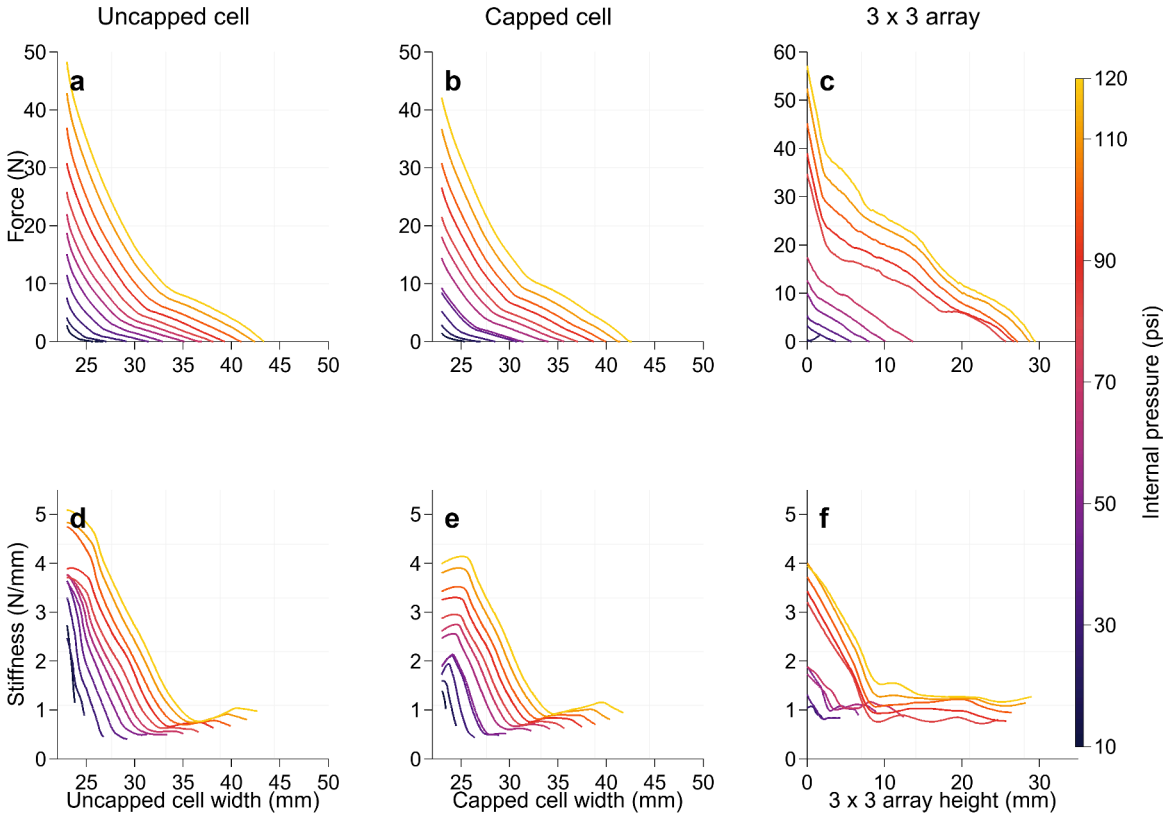

Figure 5. Pressure-dependent force and stiffness for cells and arrays. (a–c) Measured force response of the uncapped cell, capped cell, and 3×3 module array over the compression stroke. (d–f) Local stiffness computed from the corresponding force-displacement curves. Color indicates internal pressure.

2.2 Planar reconfiguration

In the planar topology, we first quantify static shape generation and then show dynamic actuation sequences for object interaction and traveling surface deformations. The planar figures are organized as a progression from quantitative surface design rules to demonstrations that exploit those rules for transport and shape display.

Static planar shape generation

The printed modules, each consisting of a 2×2 arrangement of interconnected pneumatic cells, can be attached to neighboring identical modules through modular snap-fit connections. Dome size and location are selected by choosing which module groups are pressurized.

Figure 6 shows the deformations generated using the indicated actuation patterns, which span the experimentally accessible actuation range of the array, from a 1×1 module group at the center to a 6×6 group. Larger groups could not be tested in this array because the outer border is physically constrained. Although the maximum allowable actuation pressure for the cells is 120 psi, these tests were performed at 100 psi to reduce plastic deformation and wear while still producing large deformations. This fixed-pressure comparison isolates the effect of actuation footprint, allowing Table 1 to function as a scaling map for planar feature design.

The quantitative behavior of these single-dome patterns was acquired using an Intel RealSense depth camera and is summarized in Table 1. Together, Figure 6 and Table 1 show two regimes of planar shape generation. Increasing the actuation footprint from 1×1 to 3×3 modules raises the peak height from 60 to 135 mm, whereas further expansion to 6×6 modules increases the peak height only to 150 mm, revealing a saturation imposed by the finite, constrained sheet. At the same time, the height normalized by actuation-group width decreases from 2.61 to 1.09, showing that smaller footprints produce sharper, high-aspect-ratio features whereas larger footprints produce broader features with limited additional peak height. This trade-off establishes the planar array as a spatially addressable morphing surface whose feature size and amplitude can be selected by the actuation pattern rather than by redesigning the cellular unit.

The printed modules can also render multi-dome geometries, a capability critical for using planar configurations as shape displays (*13*, *33*). We demonstrate this by specifying actuation patterns that consist of pairs of 1×1 and 2×2 groups and varying the spacing of unactuated cells between them, as shown in Figure 7 and quantified in Table 2. The paired-dome data reveal a second design rule: spatial

separation improves feature distinctness but reduces peak height. For 1×1 groups, increasing the spacing from adjacent modules to four unactuated modules reduces the maximum height from 66 to 34 mm while increasing the peak-to-valley ratio from 1.08 to 1.48, converting a nearly merged dome into two more clearly resolved features. The same coupling is seen for 2×2 groups, where adjacent groups behave as a single broad deformation, but a two-module gap produces a more separated double feature with a lower peak height. Thus, neighboring actuated regions are mechanically coupled through the continuous soft sheet, and the spacing between actuation groups provides a direct way to tune the balance between smooth blended topographies and spatially resolved surface features.

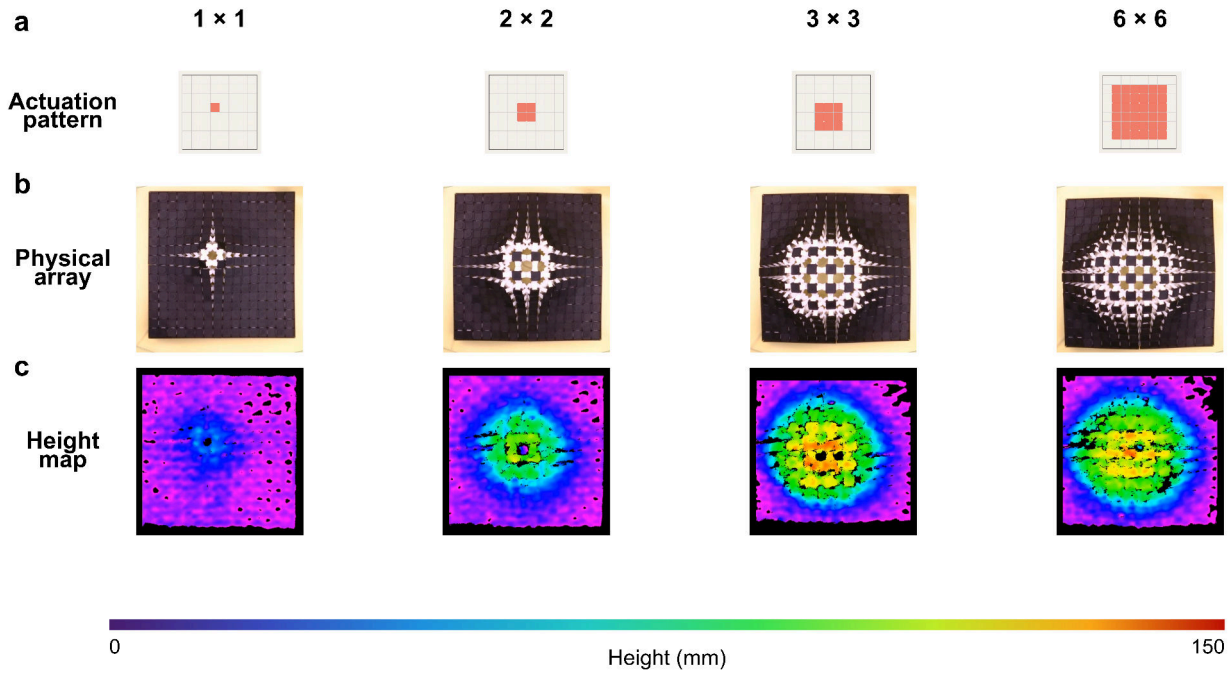

Figure 6. Single-dome shape generation in an 8×8 planar module array. (a) Actuation patterns for square groups from 1×1 to 6×6 modules. (b) Corresponding physical array deformation. (c) Height maps of the same states. Dome height increases strongly with actuation footprint before saturating for the largest groups under the fixed boundary condition.

Table 1. Single-dome scaling in the planar array at 100 psi, showing saturation of peak height and decreasing height normalized by actuation-group width as the actuated footprint increases.

Actuation group size	Max height (mm)	Height / 1×1	Height / group width
1×1	60	1.00	2.61
2×2	115	1.92	2.50
3×3	135	2.25	2.03
4×4	140	2.33	1.47
5×5	150	2.50	1.30
6×6	150	2.50	1.09

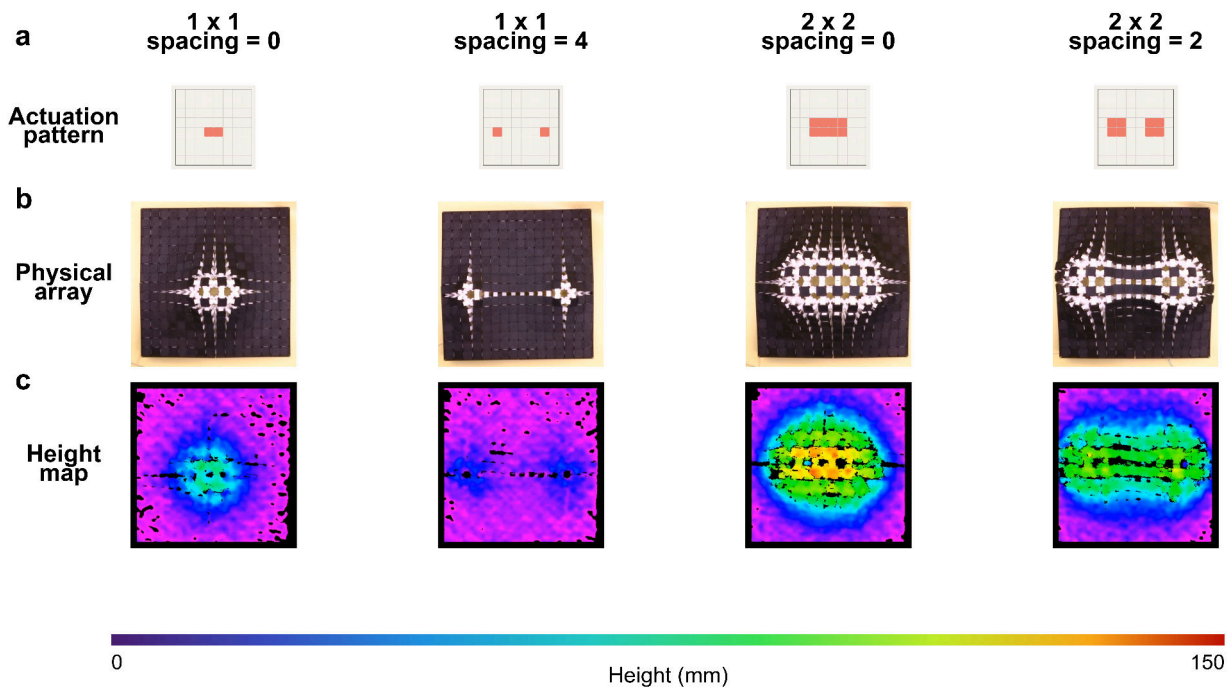

Figure 7. Spatial resolution of double-dome generation in the planar array. (a) Actuation patterns for paired 1×1 and 2×2 groups separated by increasing numbers of inactive modules. (b) Corresponding physical array deformation. (c) Height maps of the same states. Adjacent groups merge into a single broad feature, whereas larger inactive gaps produce increasingly distinct peaks with a reduced residual bridge between them.

Table 2. Double-dome spacing behavior in the planar array at 100 psi, showing the trade-off between peak height and spatial separation as inactive modules are inserted between actuated groups.

Configuration	Max height (mm)	Valley height (mm)	Peak/valley ratio
1×1 adjacent	66	61	1.08
1×1 spaced 2	46	37	1.24
1×1 spaced 4	34	23	1.48
2×2 adjacent	120	118	1.02
2×2 spaced 2	91	66	1.38

Bilayer overhang generation

The single-layer planar array generates raised features directly above actuated modules because the module bias favors convex out-of-plane buckling. We next tested whether the same cell could generate opposite curvature directions when the topology was changed. A single layer can produce an apparent depressed region indirectly, by actuating surrounding modules to raise the neighboring surface, but this approach does not provide direct and comparable control of both curvature directions.

We addressed this limitation by implementing a secondary inverted layer that provides antagonistic actuation and bidirectional intrinsic biasing, enabling both convex and concave curvature within the

same structure. Selective actuation of cells in the upper and lower layers generates local in-plane expansion and bending at specified locations, allowing opposite curvature directions to be produced within a single geometry. Using this configuration, we achieved a clear overhang geometry, shown in Figure 8, which includes both the actuation pattern and the resulting physical array. The demonstrated bilayer structure, consisting of 66 cells in total, achieved approximately 1 cm of overhang, showing that the same cell can move beyond height-field surfaces when the topology is reconfigured into opposed layers.

Planar object interaction

We next demonstrate that the planar topology can interact with objects by rolling a tennis ball using convex and concave surface deformation modes (*13*, *33*). In convex manipulation, the ball rolls away from the actuated groups that raise the surface, as shown in Figure 9. A press-fit border attached to the double-layer clips keeps the ball on the array. For concave manipulation, elevating the array on stilt-like supports allows selected actuation groups to create a gravity-assisted capture basin, causing the ball to roll toward the actuated region and remain confined by the bowl-like surface (Figure 10). Together, Figures 9 and 10 show that transport direction can be selected by presenting either a raised feature or a depressed capture region.

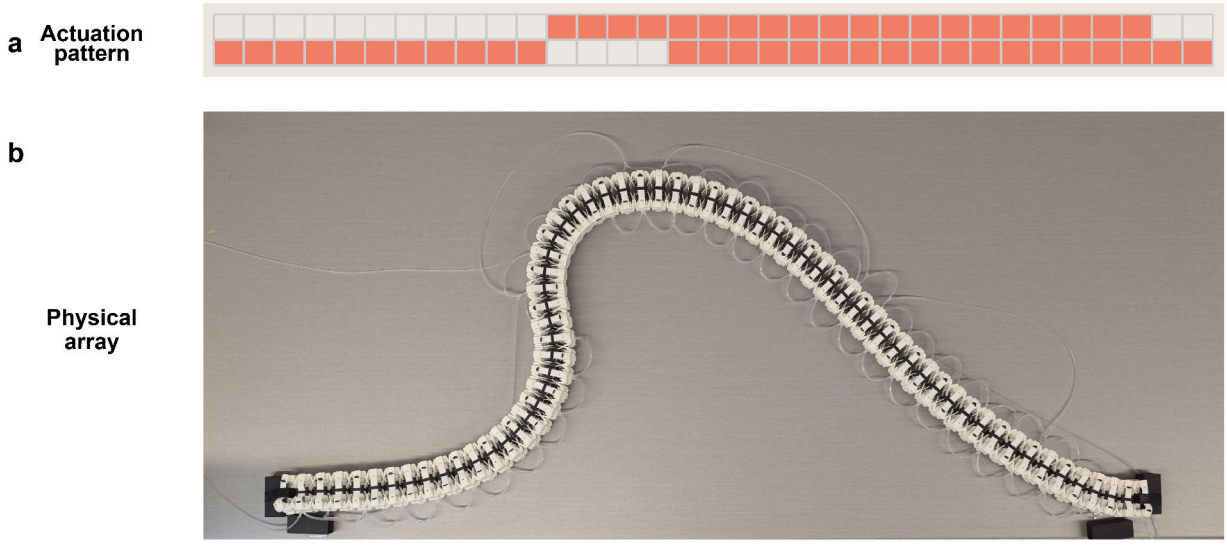

Figure 8. Bilayer overhang generation. (a) Actuation pattern for the opposed upper and lower cell layers. (b) Physical 33-cell row showing the resulting overhang. Two opposed cell layers are connected with snap-fit clips to provide antagonistic actuation and direct access to both convex and concave curvature while preserving the same repeated cellular unit.

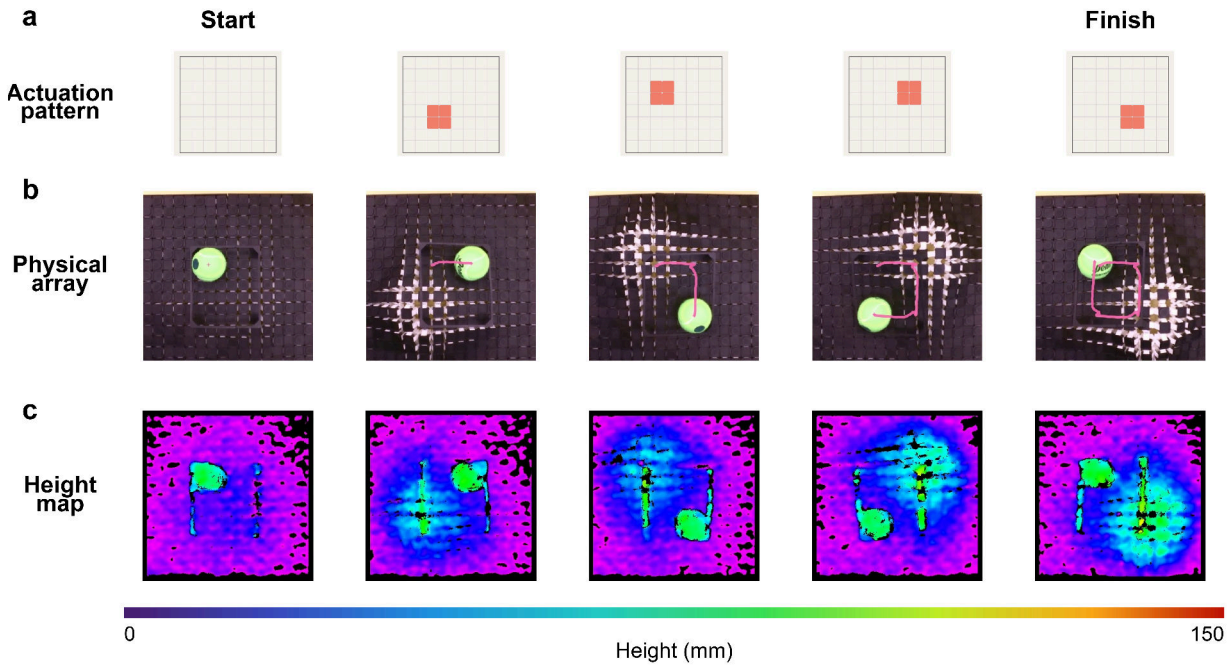

Figure 9. Convex planar object interaction. (a) Actuation-pattern sequence. (b) Physical array images showing tennis-ball motion. (c) Height maps corresponding to the same sequence. Sequential actuation of raised surface regions rolls the tennis ball away from the actuated groups while the border constrains the ball to the array.

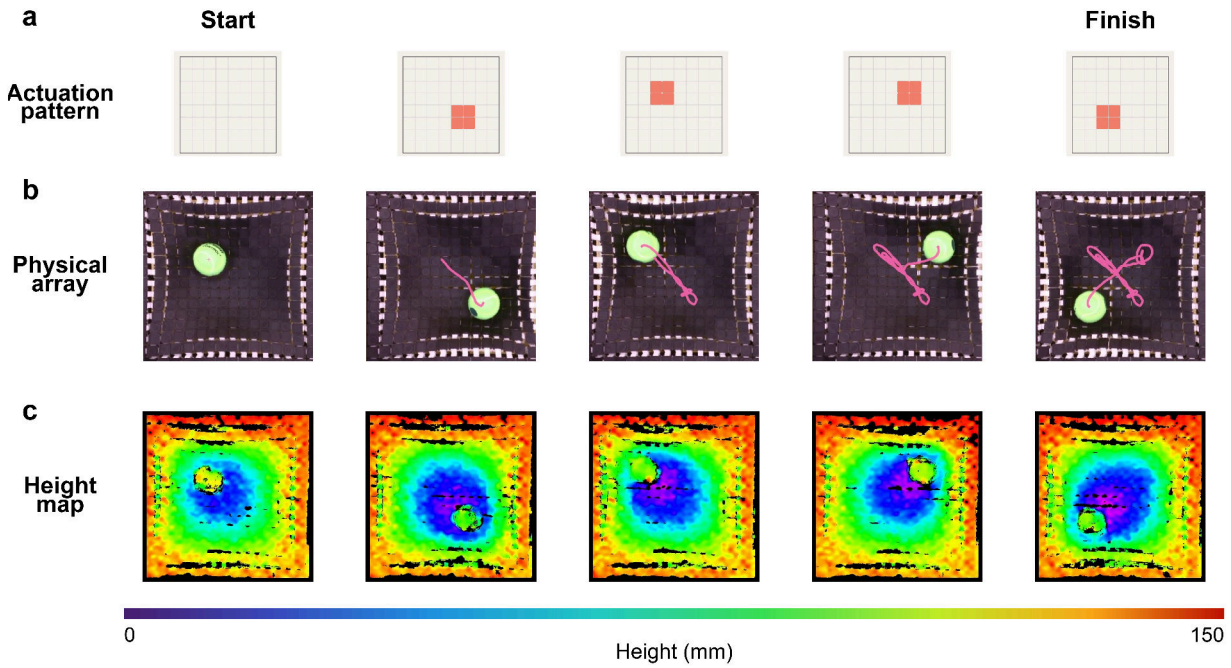

Figure 10. Concave planar object interaction. (a) Actuation-pattern sequence. (b) Physical array images showing tennis-ball motion. (c) Height maps corresponding to the same sequence. Elevating the array and actuating selected groups creates a gravity-assisted depressed region, causing the tennis ball to roll toward the actuated zone and remain captured by the bowl-like surface.

Dynamic planar shape display

The same modules can also generate traveling surface features rather than only static domes (*13*, *33–35*). We implement three actuation sequences: a wave traveling horizontally across the array, a wave traveling along the diagonal, and a wave circulating around a closed path. These three demonstrations convert the static feature rules from Figures 6 and 7 into specified time-varying trajectories, demonstrating that the surface can route deformation rather than only hold a prescribed shape.

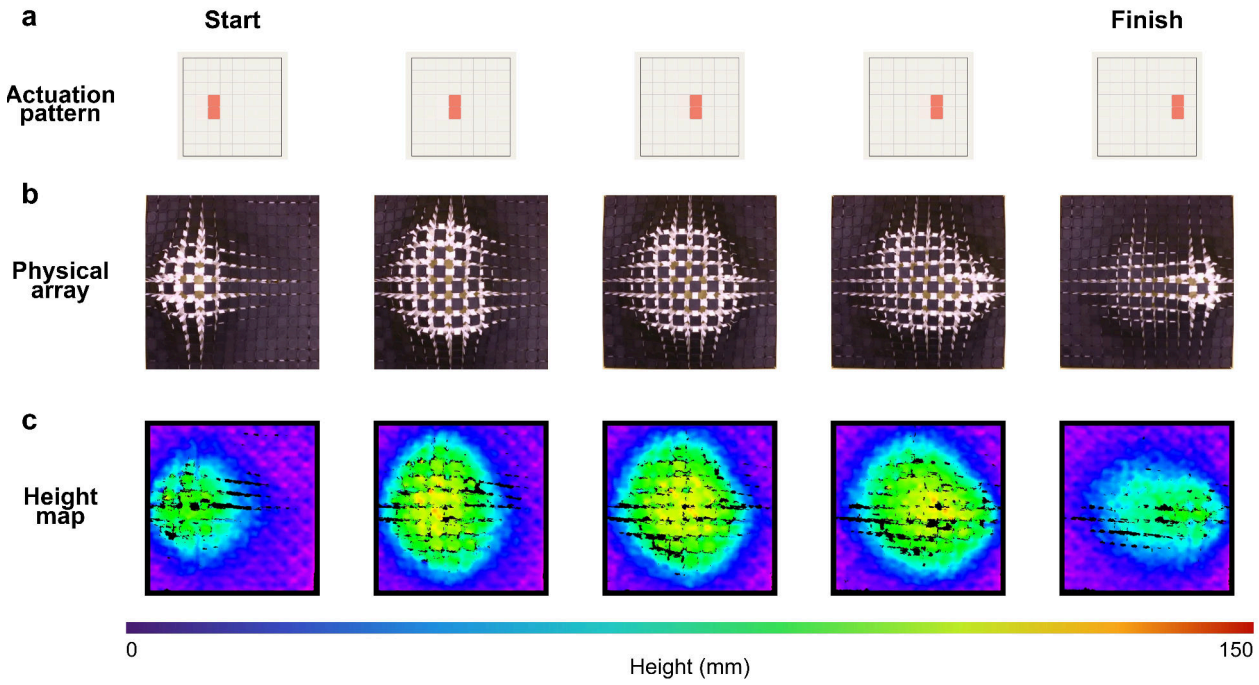

Figure 11. Traveling planar wave in the horizontal direction. (a) Actuation-pattern sequence. (b) Physical array images. (c) Height maps of the same sequence. Sequential actuation of preselected module groups translates a raised feature from left to right across the soft array.

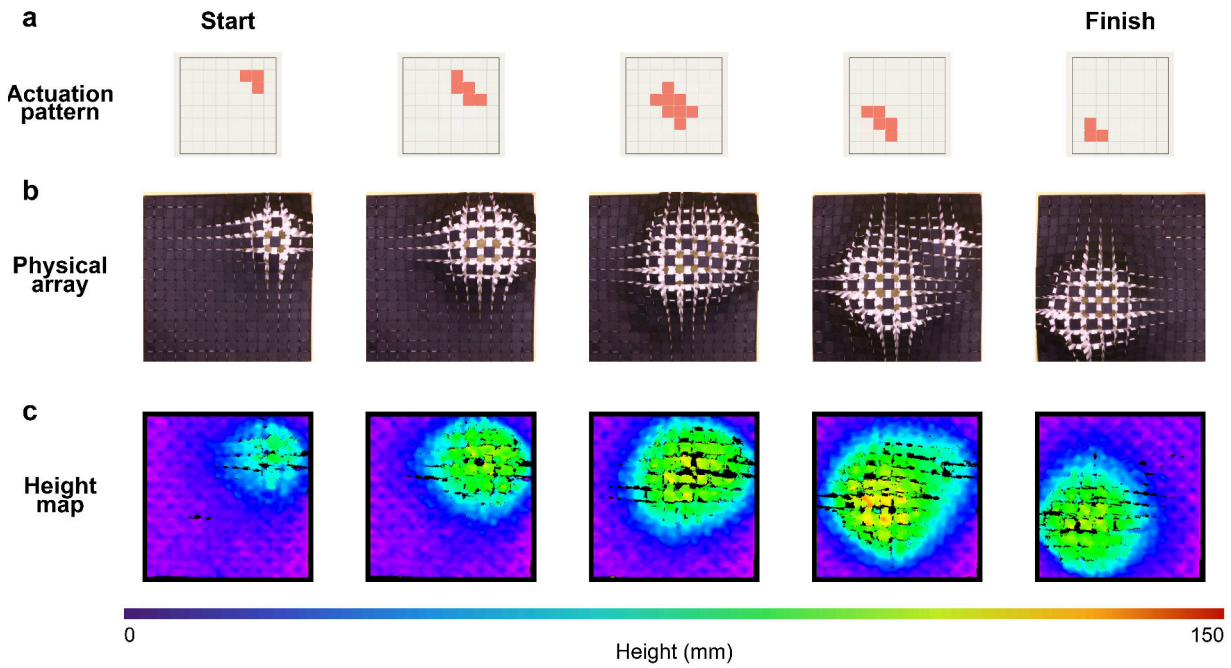

Figure 12. Traveling planar wave along the array diagonal. (a) Actuation-pattern sequence. (b) Physical array images. (c) Height maps of the same sequence. The raised feature moves across both row and column directions, demonstrating two-dimensional routing of dynamic surface deformation.

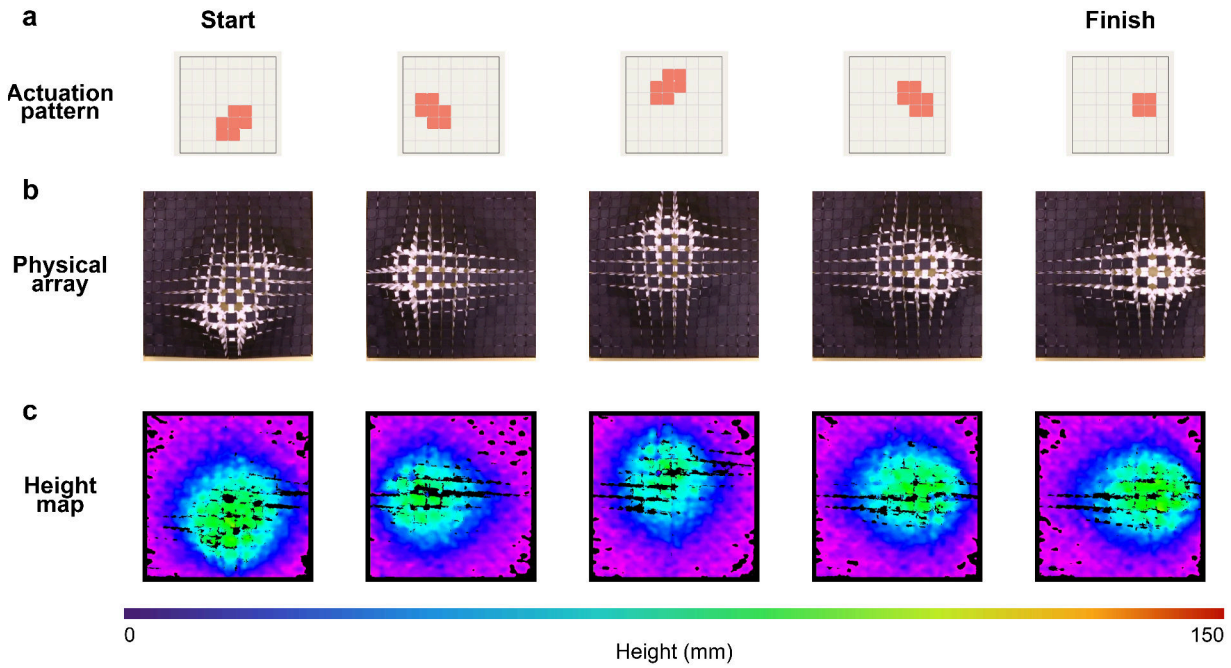

Figure 13. Circular traveling wave in the planar array. (a) Actuation-pattern sequence. (b) Physical array images. (c) Height maps of the same sequence. Sequential actuation around a closed path produces a circulating raised feature, demonstrating repeatable dynamic shape display using the same module topology.

Together, the planar demonstrations show that local actuation of repeated cells can produce both quantitative surface primitives and task-level interaction with objects. The same array can operate as a static shape display, a dynamic morphing surface, or a soft object-transport surface without changing the cell design.

2.3 Cylindrical reconfiguration

Rolling the same repeated modules into a tubular topology enables bending, object manipulation, and locomotion without redesigning the building block. A cylindrical configuration is achieved by rolling a planar array into a tube and joining the two free edges with the intermodule snap-fit connectors. We then specify actuation patterns for a 4×10 module array according to the desired deformation.

Cylindrical bending

Figure 14 shows the actuation pattern used for each C-curve direction. Actuating one side of the cylinder expands that side and bends the tube toward the opposite side. Because the cylinder contains four modules around its circumference, rotating this actuation pattern produces curvature in four Cartesian directions. To produce S-curves, the actuation pattern is split along the tube length and the two halves are actuated on opposite sides (Figure 15). Together, Figures 14 and 15 show that changing from a planar array to a cylindrical body converts the same module from a surface display element into a continuum-style bending segment without changing the cell architecture (*3*, *7*, *36*).

Continuum arm grasping

Using the same cylindrical topology, we next form a long tube-like structure that resembles a continuum arm, a class of systems widely studied in soft robotics (*17–19*, *37*). Figure 16 shows the actuation pattern used to generate the respective deformation states, demonstrating the controlled grasping, moving, and placing of an object.

To perform the manipulation sequence, the distal ring is first actuated to enlarge the opening around the test object. Actuating the body lowers the arm, and releasing the distal ring closes the end around the object. A C-curve actuation pattern then translates and lifts the grasped object before the distal ring is actuated again to release it. Figure 16 therefore uses the bending primitives from Figures 14 and 15 as a manipulation sequence, turning topology-level reconfiguration into a task-level behavior.

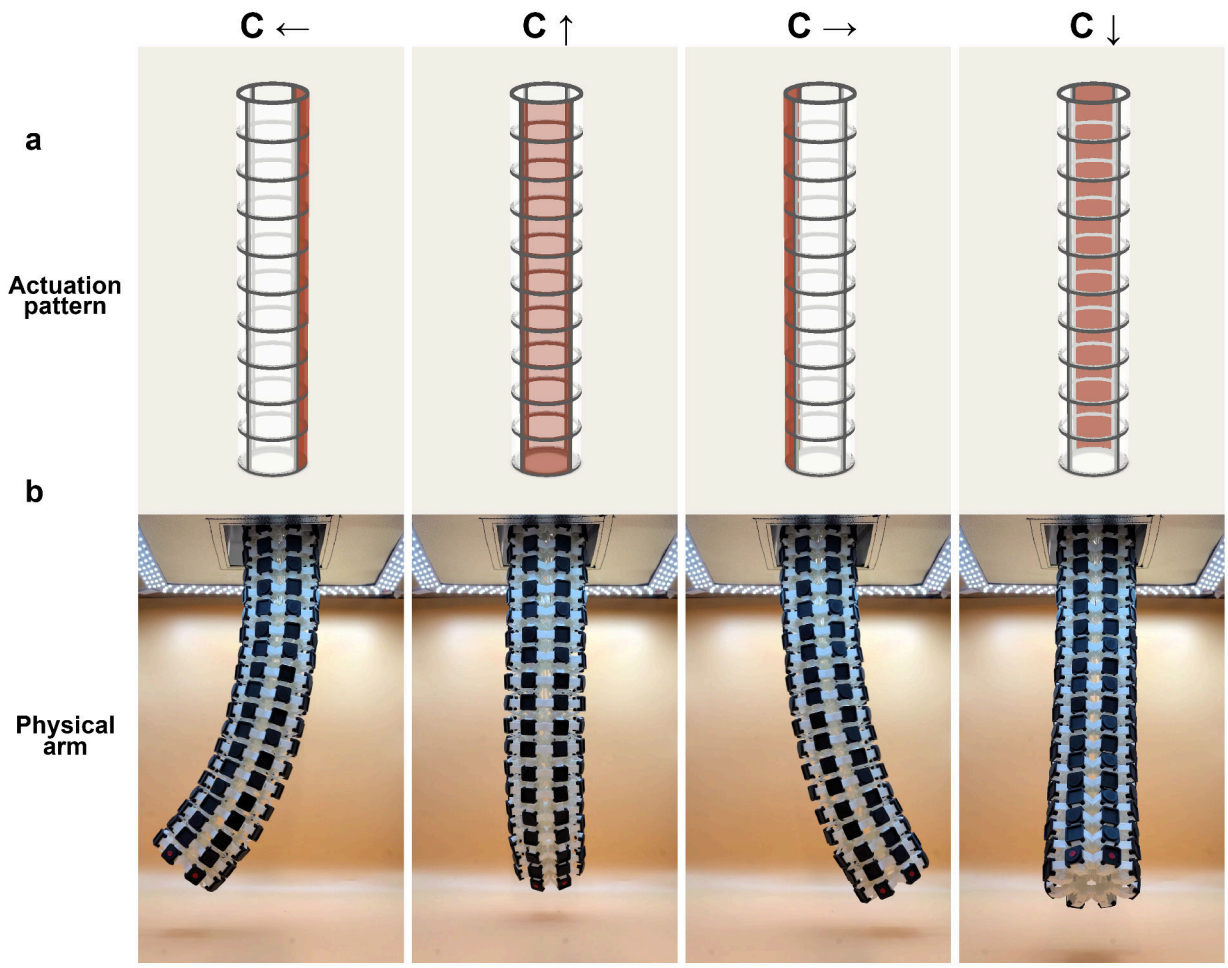

Figure 14. Cylindrical C-curve generation. (a) Actuation patterns for four bending directions around the tube circumference. (b) Corresponding physical arm images. A 4×10 module sheet is rolled into a tube and joined with snap-fit connectors; actuating one longitudinal side expands that side of the cylinder and bends the tube toward the opposite side, enabling C-curves in four directions without redesigning the module.

Peristaltic locomotion

Peristaltic locomotion is widely studied in continuum soft robotics (*20–22*). It uses repeated propagating deformation waves to move the robot body along the actuation direction. We create this wave-like propagation by defining six actuation groups, which correspond to six module groups along the robot's length, and actuating them in quick succession over repeated cycles. Six feet are press-fit into the cell cap connectors, which are designed to raise the cylindrical body off the table. These feet are fitted with TPU sleeves that increase contact friction and improve traction. Using this gait, the robot moved approximately 200 mm, as shown in Figure 17. This figure closes the loop between the traveling waves shown in the planar array and physical translation in a cylindrical body, demonstrating that sequential local inflation can be reused as a locomotion primitive.

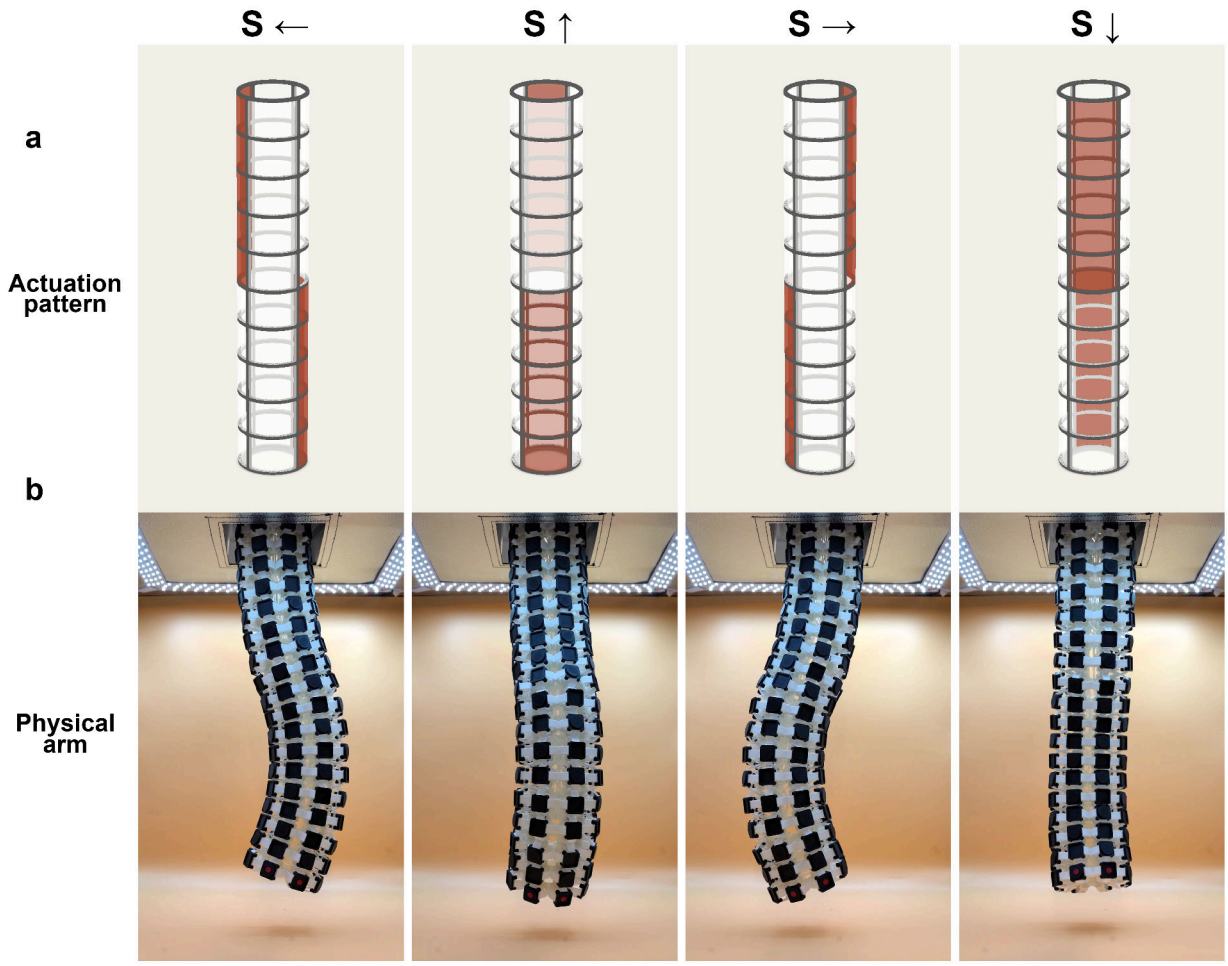

Figure 15. Cylindrical S-curve generation. (a) Actuation patterns for four S-curve directions. (b) Corresponding physical arm images. Splitting the actuation pattern along the tube length and actuating opposite sides in the two segments produces an S-shaped deformation using the same cylindrical assembly.

Self-rolling locomotion

Self-rolling locomotion is also achieved using cylindrical bodies assembled from the same modules. Self-rolling of cylindrical soft bodies has been studied in prior soft-robotic systems, and we use a sequential gait to produce rolling here (*23*). Figure 18 shows the actuation gait applied to a wheel-like configuration with six modules around the circumference. The wheel starts in an unactuated state, and two opposite module groups are then actuated with the upper group facing the direction of locomotion. This lengthens the wheel into an oval shape, shifts the center of mass away from the contact point, and produces rolling. Repeating this sequence produces sustained locomotion, showing that the cylindrical topology can support both substrate-based peristalsis and body-scale rolling from the same repeated module.

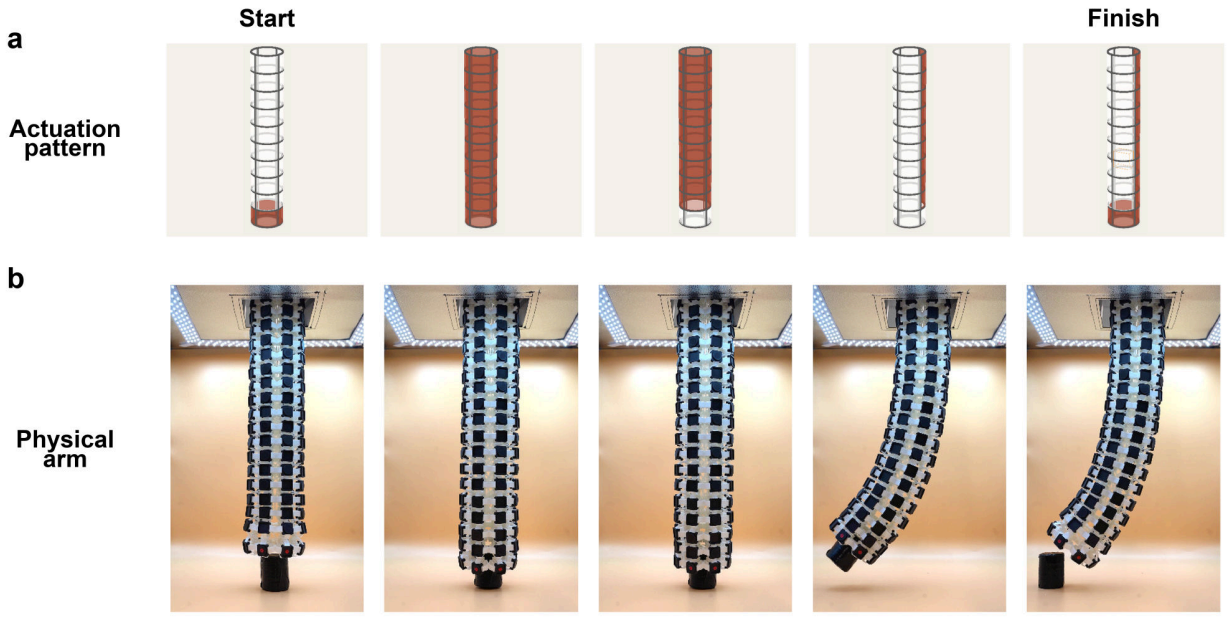

Figure 16. Continuum-arm object manipulation using the cylindrical topology. (a) Actuation-pattern sequence. (b) Physical arm images showing the corresponding manipulation states. The distal ring opens to receive the object, the body lowers around it, the ring closes to grasp it, and a C-curve actuation pattern transports and releases the object at a new location.

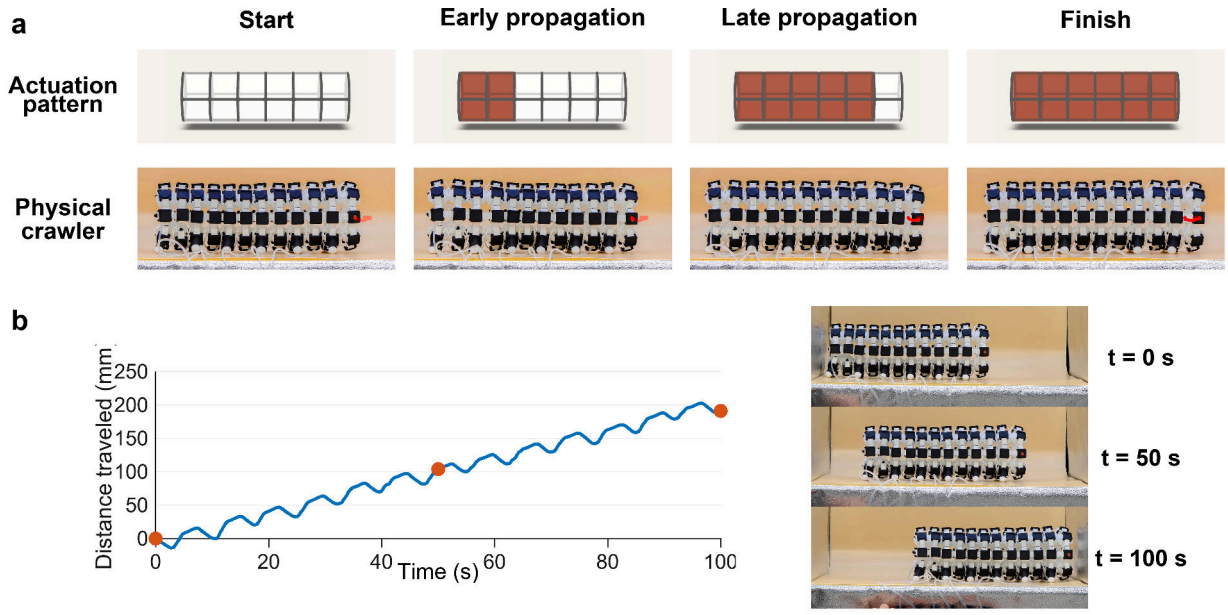

Figure 17. Peristaltic locomotion from the cylindrical topology. (a) Actuation-pattern and physical-crawler sequence for one propagating wave. (b) Distance traveled over time with representative physical snapshots at $t = 0$, 50, and 100 s. Six actuation groups are driven in sequence to create a traveling deformation wave along the robot body, and press-fit feet with high-friction sleeves provide surface traction for repeated forward motion.

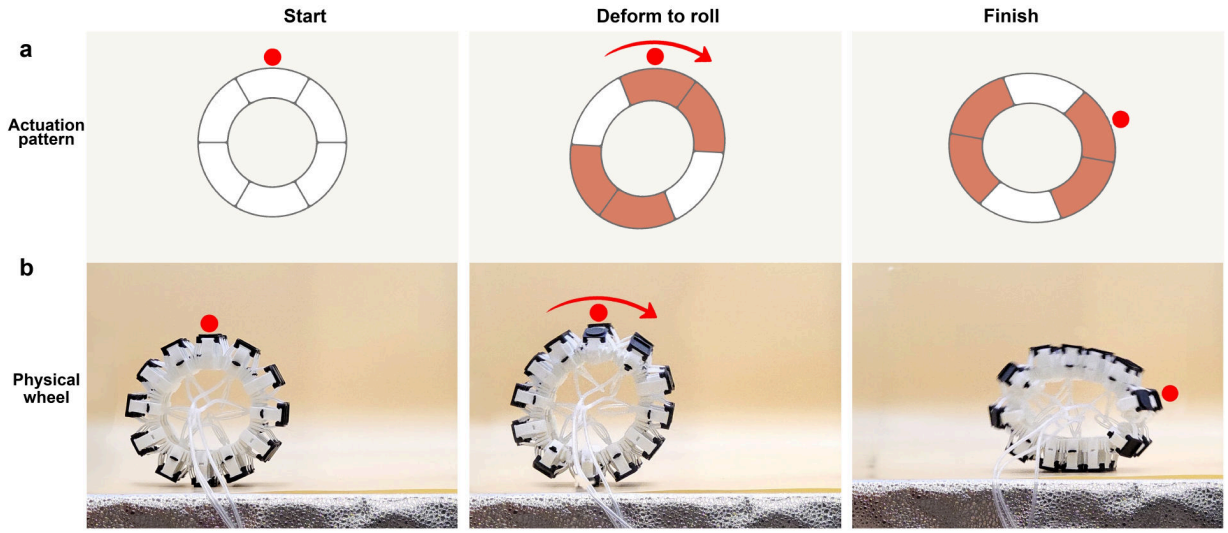

Figure 18. Self-rolling locomotion from a wheel-like cylindrical assembly. (a) Circumferential actuation-pattern sequence. (b) Physical rolling snapshots of the wheel-like body. Opposed module groups are actuated in a repeated sequence offset around the circumference, shifting the center of mass relative to the contact point and producing rolling motion.

The cylindrical demonstrations show that the architecture is not limited to planar shape display. By changing only the assembly topology and actuation pattern, the same repeated cell becomes part of a continuum-style bending body, a simple manipulator, a peristaltic crawler, or a rolling robot.

3 Discussion

This work establishes a topology-reconfigurable soft robotic architecture in which one monolithically printed pneumatic unit can be reconfigured into distinct robotic topologies. The central result is that local pressure-driven expansion can be converted by module-scale bias into controlled three-dimensional deformation. That mechanism allows the same repeated unit to support planar surface morphing, object interaction, continuum-style bending, grasping, peristaltic locomotion, and self-rolling locomotion. Relative to modular soft building-block robots and voxel robots, the system emphasizes continuous, locally addressable shape formation from a monolithic pneumatic cell; relative to soft reconfigurable surfaces, it also functions as a reconfigurable robot body (*5–8*). In this sense, the system's function is selected by assembly topology and actuation pattern.

The experiments also identify design rules for using the architecture as a controlled morphing surface. In single-dome patterns, increasing the actuated footprint increases height only up to a saturation regime, while the height normalized by group width decreases as the feature broadens. In double-dome patterns, larger spacings of unactuated cells improve feature separation but reduce peak height. These

trends show that neighboring actuated regions are mechanically coupled through the continuous sheet, so spatial resolution and amplitude cannot be chosen independently. This coupling limits high-resolution display, but it is also the source of the smooth, continuous shapes that distinguish the architecture from discrete pin- or voxel-like systems.

The cylindrical demonstrations show why topology-level reconfiguration is important. Rolling the same modules into tubes changes the available deformation modes without changing the cell architecture: local expansion becomes directional bending, sequential expansion becomes peristaltic transport, and circumferentially offset expansion becomes rolling. This provides a route to building families of soft robots from a common manufacturable unit rather than redesigning the cellular actuator and connection scheme for each task.

The next step is to move from prescribed demonstrations to integrated robotic control. The present prototypes are tethered and use manually assigned actuation patterns, but the architecture is compatible with electronically addressed pneumatic actuation, embedded sensing, and closed-loop control. Pairing embedded actuation with sensing of external forces, curvature, and vision-based feedback would allow a controller to infer body state and adjust actuation in response to contact, deformation, and task demands. With this integration, the architecture could become a soft robot body whose shape, gait, and task behavior are specified and regulated in real time.

Several limitations remain. The current modules require pneumatic tubing, external pressure control, and manual assembly, which constrain the scale and speed of reconfiguration. The planar arrays were evaluated under fixed boundary conditions and with a limited set of actuation footprints, so larger arrays will be needed to characterize spatial resolution, edge effects, and multi-feature interference. The bilayer overhang demonstration shows a path toward three-dimensional surfaces with locally opposed actuation, but the present prototype is limited to 66 cells across both layers and produces a modest overhang. Extending this concept from a proof-of-principle row to a larger surface would allow overhangs to be generated across a broader two-dimensional area. More broadly, integrated sensing, closed-loop control, and algorithmic pattern planning would allow the same cellular architecture to move from proof-of-principle demonstrations toward autonomous soft robotic systems that can be configured, sensed, controlled, and repurposed for changing tasks.

4 Materials and Methods

Cell design and fabrication

The cell integrates the Sarrus linkage and pneumatic actuator in a monolithically 3D-printed unit (Figure 1). Several forms of printed actuation are available, including 3D-printed shape-memory actuators (*38*), liquid-crystal-elastomer actuators (*39*), dielectric-elastomer actuators (*40*), and bimorph electrothermal actuators (*41*). We use 3D-printed pneumatic actuation because it provides reversible motion with large forces over substantial displacements (*42*, *43*). The linkage members and flexural joints are fabricated from a single soft material, eliminating multimaterial printing and reducing part count. This design transforms the Sarrus linkage into a compliant mechanism, avoiding the backlash, frictional wear, and mechanical looseness associated with discrete pin joints (*44*, *45*).

The actuator geometry was chosen to be compatible with monolithic single-material 3D printing. Multiple soft pneumatic architectures are possible, including linear expansion actuators (*42*) and bending-based designs (*43*, *46*). Because the structure is printed layer by layer from the build plate upward, unsupported overhangs would require removable supports, and support material cannot be extracted from sealed pneumatic chambers. The feasible design space is therefore limited to actuator geometries that are self-supporting in their print orientation. We use a PneuNet bending actuator integrated within the lower portion of the cell; when actuated, it opens the Sarrus legs and produces in-plane expansion. Here, linkage refers to the Sarrus linkage alone, cell refers to the monolithically printed unit that combines the linkage and actuator, and module refers to a 2×2 arrangement of four interconnected cells. The cap minimizes gaps between adjacent cells during object interaction and enables the double-layer configuration.

Module architecture and directional biasing

We grouped 2×2 arrangements of cells into modules (Figure 2) to reduce tubing complexity and introduce a built-in directional bending bias. Individual actuation of each cell would require many pneumatic inputs. In addition, if each cell underwent pure in-plane expansion, a planar array would buckle out of plane in an uncontrolled direction and would require an external biasing mechanism.

By integrating pneumatic channels between adjacent cells within each module, all four cells are connected to a single pneumatic input, simplifying actuation. At the same time, the integrated pneumatic channels introduce a built-in mechanical bias that controls the bending direction. The connections between adjacent cells consist of two thin structural legs in the upper region and two thicker legs in the lower PneuNet actuation region. In the unactuated state these legs are nearly parallel, as shown in the cross-section in Figure 2d; during inflation, the bulging pneumatic pockets rotate these legs into the upright-V and inverted-V linkage leg pairs highlighted in the 80 psi images in Figure 2a,b. The upper region forms a more compliant upright-V leg pair, while the lower cross-cell pneumatic channel forms a stiffer inverted-V leg pair. As a result, expansion is dominated by the more compliant upright-V leg pair, producing a consistent convex bending direction across the module. This built-in asymmetry removes the need for any additional biasing mechanism to control the buckling direction. We also carry this biasing principle between modules, attaching the stiffer bottom legs of adjacent modules with a rigid snap-fit connector. This limits opening of the inverted-V leg pair at the intermodule level, similar to the intramodule level.

Acknowledgements

The authors thank Worcester Polytechnic Institute for institutional support.

Funding

This work was partially supported by the National Science Foundation (NSF).

Author contributions

A.N.P. performed the research and prepared the manuscript. P.R. and C.D.O. supervised the work and provided feedback on the manuscript.

Competing interests

The authors declare no competing interests.

Data availability

All data needed to evaluate the conclusions are included in the paper. Additional raw data are available from the corresponding author upon reasonable request.

Code availability

Figure-generation code and analysis scripts are available from the corresponding author upon reasonable request.

Additional information

Correspondence and requests for materials should be addressed to A.N.P.

References

1. R. L. Truby, Designing Soft Robots as Robotic Materials. *Accounts of Materials Research* **2**, 854–857 (Oct. 2021).
2. D. Hughes, C. Heckman, N. Correll, Materials that make robots smart. *The International Journal of Robotics Research* **38**, 1338–1351 (Oct. 2019).
3. J. Wang *et al.*, Robo-Matter towards reconfigurable multifunctional smart materials. *Nature Communications* **15**, 8853 (Oct. 2024).
4. S. M. B. P. Samarakoon, M. A. V. J. Muthugala, M. R. Elara, Tiling Robotics: A New Paradigm of Shape-Morphing Reconfigurable Robots. *Advanced Intelligent Systems* **7**, 2400417 (2025).
5. M. G. B. Atia, A. Mohammad, A. Gameros, D. Axinte, I. Wright, Reconfigurable Soft Robots by Building Blocks. *Advanced Science* **9**, 2203217 (Nov. 2022).
6. J. Legrand, S. Terryn, E. Roels, B. Vanderborght, Reconfigurable, Multi-Material, Voxel-Based Soft Robots. *IEEE Robotics and Automation Letters* **8**, 1255–1262 (Mar. 2023).

7. G. Liang, A. J. Ijspeert, M. Yim, T. L. Lam, Modular reconfigurable robots: Toward on-demand multifunctional applications. *Science Robotics* **11**, eadz1999 (Feb. 2026).

8. M. A. Robertson, M. Murakami, W. Felt, J. Paik, A Compact Modular Soft Surface With Reconfigurable Shape and Stiffness. *IEEE/ASME Transactions on Mechatronics* **24**, 16–24 (Feb. 2019).

9. A. F. Siu, E. J. Gonzalez, S. Yuan, J. B. Ginsberg, S. Follmer, presented at the Proceedings of the 2018 CHI Conference on Human Factors in Computing Systems, pp. 1–13.

10. K. Nakagaki *et al.*, presented at the Proceedings of the Thirteenth International Conference on Tangible, Embedded, and Embodied Interaction, pp. 615–623.

11. Y.-L. Feng, R. L. Peiris, C. L. Fernando, K. Minamizawa, presented at the Haptics: Science, Technology, and Applications, ed. by D. Prattichizzo, H. Shinoda, H. Z. Tan, E. Ruffaldi, A. Frisoli, pp. 180–192.

12. A. Steed, E. Ofek, M. Sinclair, M. Gonzalez-Franco, A mechatronic shape display based on auxetic materials. *Nature Communications* **12**, 4758 (Aug. 2021).

13. B. K. Johnson *et al.*, A multifunctional soft robotic shape display with high-speed actuation, sensing, and control. *Nature Communications* **14**, 4516 (July 2023).

14. Y. Wang, K. Wang, Z. Wang, K. Perlin, presented at the Proceedings of the Nineteenth International Conference on Tangible, Embedded, and Embodied Interaction, pp. 1–11.

15. D. R. Sahoo, K. Hornbæk, S. Subramanian, presented at the Proceedings of the 2016 CHI Conference on Human Factors in Computing Systems, pp. 3767–3780.

16. S.-Y. Jang *et al.*, Dynamically reconfigurable shape-morphing and tactile display via hydraulically coupled mergeable and splittable PVC gel actuator. *Science Advances* **10**, eadq2024 (Sept. 2024).

17. X. Wang, Q. Lu, D. Lee, Z. Gan, N. Rojas, A Soft Continuum Robot With Self-Controllable Variable Curvature. *IEEE Robotics and Automation Letters* **9**, 2016–2023 (Mar. 2024).

18. J. Santoso, C. D. Onal, An Origami Continuum Robot Capable of Precise Motion Through Torsionally Stiff Body and Smooth Inverse Kinematics. *Soft Robotics* **8**, 371–386 (Aug. 2021).

19. A. R. Elchrif, M. I. Awad, S. A. Maged, A. Ramzy, Modular soft pneumatic actuator mimics elephant trunk locomotion. *Scientific Reports* **14**, 24169 (Oct. 2024).

20. S. Seok *et al.*, Meshworm: A Peristaltic Soft Robot With Antagonistic Nickel Titanium Coil Actuators. *IEEE/ASME Transactions on Mechatronics* **18**, 1485–1497 (Oct. 2013).

21. T. Yanagida, K. Adachi, M. Yokojima, T. Nakamura, presented at the 2012 IEEE/RSJ International Conference on Intelligent Robots and Systems, pp. 2935–2940.

22. Y. Peng, H. Nabae, Y. Funabora, K. Suzumori, Controlling a peristaltic robot inspired by inchworms. *Biomimetic Intelligence and Robotics* **4**, 100146 (Mar. 2024).

23. W.-B. Li, W.-M. Zhang, H.-X. Zou, Z.-K. Peng, G. Meng, A Fast Rolling Soft Robot Driven by Dielectric Elastomer. *IEEE/ASME Transactions on Mechatronics* **23**, 1630–1640 (Aug. 2018).

24. A. Everitt, J. Alexander, 3D Printed Deformable Surfaces for Shape-Changing Displays. *Frontiers in Robotics and AI* **6**, 80 (Aug. 2019).

25. X. Xia, C. M. Spadaccini, J. R. Greer, Responsive materials architected in space and time. *Nature Reviews Materials* **7**, 683–701 (Sept. 2022).

26. T. Chen, J. Panetta, M. Schnaubelt, M. Pauly, Bistable auxetic surface structures. *ACM Transactions on Graphics* **40**, 1–9 (Aug. 2021).

27. T.-U. Lee *et al.*, Self-locking and stiffening deployable tubular structures. *Proceedings of the National Academy of Sciences* **121**, e2409062121 (Oct. 2024).

28. Y. Yang, X. Zhang, P. Maiolino, Y. Chen, Z. You, Linkage-based three-dimensional kinematic metamaterials with programmable constant Poisson's ratio. *Materials & Design* **233**, 112249 (Sept. 2023).

29. H. D. McClintock *et al.*, A Fabrication Strategy for Reconfigurable Millimeter-Scale Metamaterials. *Advanced Functional Materials* **31**, 2103428 (Nov. 2021).

30. A. F. Minori *et al.*, Reversible actuation for self-folding modular machines using liquid crystal elastomer. *Smart Materials and Structures* **29**, 105003 (Oct. 2020).

31. H. C. Lee *et al.*, A fabrication strategy for millimeter-scale, self-sensing soft-rigid hybrid robots. *Nature Communications* **15**, 8456 (Sept. 2024).

32. S. Russo, T. Ranzani, J. Gafford, C. Walsh, R. Wood, presented at the 2016 IEEE International Conference on Robotics and Automation (ICRA), pp. 750–757.

33. K. Liu, F. Hacker, C. Daraio, Robotic surfaces with reversible, spatiotemporal control for shape morphing and object manipulation. *Science Robotics* **6**, eabf5116 (Apr. 2021).

34. Y. Bai *et al.*, A dynamically reprogrammable surface with self-evolving shape morphing. *Nature* **609**, 701–708 (Sept. 2022).

35. X. Ni *et al.*, Soft shape-programmable surfaces by fast electromagnetic actuation of liquid metal networks. *Nature Communications* **13**, 5576 (Sept. 2022).

36. H. Gu *et al.*, Self-folding soft-robotic chains with reconfigurable shapes and functionalities. *Nature Communications* **14**, 1263 (Mar. 2023).

37. X. Wang, N. Rojas, presented at the 2024 IEEE 7th International Conference on Soft Robotics (RoboSoft), pp. 705–710.

38. Q. Ge *et al.*, Multimaterial 4D Printing with Tailorable Shape Memory Polymers. *Scientific Reports* **6**, 31110 (Aug. 2016).

39. F. Zhai *et al.*, 4D-printed untethered self-propelling soft robot with tactile perception: Rolling, racing, and exploring. *Matter* **4**, 3313–3326 (Oct. 2021).

40. T. B. Palmić, J. Slavič, Single-process 3D-printed stacked dielectric actuator. *International Journal of Mechanical Sciences* **230**, 107555 (Sept. 2022).

41. G. Krivic, J. Slavič, Single-process 3D-printed bimorph electrothermal soft actuators. *International Journal of Mechanical Sciences* **297-298**, 110299 (July 2025).

42. M. Schaffner *et al.*, 3D printing of robotic soft actuators with programmable bioinspired architectures. *Nature Communications* **9**, 878 (Feb. 2018).

43. B. Mosadegh *et al.*, Pneumatic Networks for Soft Robotics that Actuate Rapidly. *Advanced Functional Materials* **24**, 2163–2170 (Apr. 2014).

44. S. P. Jagtap, B. B. Deshmukh, S. Pardeshi, Applications of compliant mechanism in today's world – A review. *Journal of Physics: Conference Series* **1969**, 012013 (July 2021).

45. M. Ling, L. L. Howell, J. Cao, G. Chen, Kinetostatic and Dynamic Modeling of Flexure-Based Compliant Mechanisms: A Survey. *Applied Mechanics Reviews* **72**, 030802 (May 2020).

46. A. D. Marchese, R. K. Katzschmann, D. Rus, A Recipe for Soft Fluidic Elastomer Robots. *Soft Robotics* **2**, 7–25 (Mar. 2015).